

Water vapor mass transfer in alginate–graphite bio-based hydrogel for atmospheric water harvesting

Original

Water vapor mass transfer in alginate–graphite bio-based hydrogel for atmospheric water harvesting / Gentile, Vincenzo; Calò, Matteo; Bozlar, Michael; Simonetti, Marco; Meggers, Forrest. - In: INTERNATIONAL JOURNAL OF HEAT AND MASS TRANSFER. - ISSN 0017-9310. - ELETTRONICO. - 219:(2024). [10.1016/j.ijheatmasstransfer.2023.124794]

Availability:

This version is available at: 11583/2985685 since: 2024-02-05T15:12:07Z

Publisher:

Elsevier

Published

DOI:10.1016/j.ijheatmasstransfer.2023.124794

Terms of use:

This article is made available under terms and conditions as specified in the corresponding bibliographic description in the repository

Publisher copyright

(Article begins on next page)



Water vapor mass transfer in alginate–graphite bio-based hydrogel for atmospheric water harvesting

Vincenzo Gentile^{a,c,*}, Matteo Calò^a, Michael Bozlar^{b,c}, Marco Simonetti^a, Forrest Meggers^c

^a Department of Energy, Politecnico di Torino Corso Duca degli Abruzzi 24, Turin, Italy

^b Department of Mechanical & Aerospace Engineering, The University of Texas at Arlington, Arlington, TX 76019 USA

^c School of Engineering and Applied Science, Andlinger Center for Energy and the Environment, Princeton University, Princeton, NJ 08544 USA

ARTICLE INFO

Keywords:

Water vapor diffusion
Alginate hydrogel
Biopolymer
Diffusion kinetics
Atmospheric water harvesting
Optimal thermal cycle

ABSTRACT

This study presents experimental and theoretical investigations on water vapor mass transfer of a novel hydrogel compound based on alginate and graphite. This hydrogel enables rapid, reproducible, and thermally driven cycles for the adsorption and desorption of water vapor from ambient air for atmospheric water harvesting applications. We study the impacts of hydrogel composition on sorption capacity and kinetics using sorption/regeneration experiments under various environmental conditions. Theoretical models based on Fick's law of diffusion and Linear Driving Force are developed and validated with experiments to optimize thermal cycling conditions within the temperature range of 20–100 °C. The bio-based hydrogel exhibited remarkable water uptake, ranging from 0.5 to 0.9 g/g, with RH below 30 and 50 %, respectively. This low-humidity setting enables a water production rate of 1.6–2.9 L/kg of sorbent per day with a low-grade thermal regeneration (60–100 °C). Natural graphite microparticles improve water vapor release kinetics during regeneration, with an effective diffusivity coefficient of around 10^{-11} m²/s.

1. Introduction

1.1. Problem statement

Atmospheric water harvesting (AWH) is a promising solution to produce water when natural sources such as surface freshwater are unavailable [1–5]. AWH involves the separation and condensation of moisture from the atmosphere. This technique offers a promising option for desalination in situations where the distance from the sea or brackish aquifer makes other methods less competitive, providing an effective solution to access freshwater in remote locations [4,6–9].

One approach for AWH involves lowering the air temperature below the dew point through refrigerant cooling cycles [5,8,10] or thermoelectric coolers [11,12]. These systems are typically suitable for humid environments and consume more than 0.3–1 kWh/L of electricity, with an expected loss of efficiency in dry climates [5,10,13].

In contrast, another method employs sorbents that cyclically capture (adsorb/absorb) and release (desorb) moisture from the air [10,14–16].

While the wetting stage occurs naturally due to weak intermolecular forces (e.g., van der Waals and dispersion forces [17,18]) between polar water molecules and the sorbent, the drying stage necessitates an external heat source to activate and drive material regeneration. The

energetic demand for sorbent regeneration is within 10–40 kJ mol⁻¹ [17, 18]. Interestingly, despite the distinct physics involving desorption and liquid/vapor phase change, the heat associated with moisture sorption and water vaporization heat (2250–2500 kJ kg⁻¹) are comparable [18]. On the other hand, freshwater produced through membrane desalination, despite the concerns related to environmental issues [19–21], has three orders of magnitude less energy demand (1–3 kWh m⁻³ [22] electricity consumption). The remarkable difference originates from the inherent disparities between the two approaches: one process involves the phase change of water, while the other maintains the water in its liquid state.

Nevertheless, numerous studies explore integrating AWH and renewable heat sources, such as solar thermal energy and waste heat, to favor more sustainable water production [23–31]. We have demonstrated in an earlier study that an isothermal regeneration driven through co-located heat and mass transfer contributes to reducing energy consumption (1 kWh per liter of water) [27]. It was possible to produce fresh water with low-grade heat from solar energy using a heat and mass exchanger based on silica gel operated in dry climates. Given the silica gel's low water uptake potential, the system's daily water productivity is low (0.1 L/kg_{silica gel}/day). The daily production of 25 kg of silica gel was 1.5–3.3 L/day.

* Corresponding author at: Department of Energy, Politecnico di Torino, Corso Duca degli Abruzzi 24, Turin, Italy.

<https://doi.org/10.1016/j.ijheatmasstransfer.2023.124794>

Received 21 August 2023; Received in revised form 27 September 2023; Accepted 3 October 2023

Available online 31 October 2023

0017-9310/© 2023 The Authors. Published by Elsevier Ltd. This is an open access article under the CC BY license (<http://creativecommons.org/licenses/by/4.0/>).

New performing sorbents are then required to meet both energy efficiency requirements and daily production. The ideal sorbent for AWH exhibits high moisture uptake ($g_{\text{water}}/g_{\text{dry-sorbent}}$) and rapid material charging/discharging cycles. Further, thermally activated cycles are more convenient when the regeneration temperature is low to enable solar thermal energy or waste heat exploitation. At the same time, higher temperatures accelerate desorption kinetics, while to fulfill equilibrium uptakes may require a long time. An optimal trade-off between the sorbent's water uptake capacity and kinetics is required.

The literature presents multiple examples of sorbents [10,14–16,32] exhibiting some of those characteristics. The sorbent manufacturing practice that achieved the highest water uptakes is impregnating porous sorbent or polymers with hygroscopic salts. For example, in many earlier studies, porous nano-carbon structures were soaked in aqueous solutions of LiCl, CaCl₂, and MgSO₄ with concentrations mostly close to the saturation level (~40–50 % in mass). Examples of such systems include carbon nanofibers [31,2,33,24,34], carbon nanotubes [35,36], and lithium-based nanospheres [37]. Other options based on a similar approach involve sorbents such as hydrophilic graphene oxide [33], SiO₂ [39], and Metal-Organic Frameworks (MOFs) [30,32,38]. Increasing salt confinement in the structure increases equilibrium moisture uptake, and hygroscopic supports like composites based on polymers [30,31,35,36,39,25,40–42] or hydrogels [41,43–48] have shown superior results using similar proportions of LiCl and CaCl₂.

Although higher salt concentration improves the equilibrium uptake at low humidity conditions, it may negatively affect the kinetics or required regeneration temperature. Water uptakes are usually between 0.4–0.7 g/g when RH is below 50 %. When RH is higher, taking advantage of salt deliquescence, values overcome the unity, while equilibration times are typically higher than 400–600 min and regeneration temperature around 90–140 °C.

Another crucial aspect is the biocompatibility of materials when producing drinkable water from the available moisture in the atmosphere. Favoring salt deliquescent state, if not under control, results in leakage from the porous substrate. The intrinsic corrosive nature of CaCl₂ and the toxicity of LiCl pose questions about their use at high concentrations for long-term applications in a real engineered system. The leaching out of chemicals or impurities into the water from the sorbent or other components, such as tanks, pipes, filters, and other surfaces coming in contact with the harvested water, can compromise its safety and make it unsuitable for drinking or other uses. Therefore, sorbent design/selection must consider those aspects, especially because continuous cycling of the sorbent can degrade its structure. If the sorbent material is designed with harsh or not biocompatible chemicals, the risk of contamination can be problematic for human use.

Considering this broad point of view, this paper focuses on natural hydrogels as a sorbent solution for AWH applications.

Natural hydrogels encompass water-based polymers derived from monomers that comprise natural proteins and polysaccharides such as starch, agar, chitosan, and alginate [49,50]. Alginates [51], in particular, have found widespread applications in drug delivery [52,53], tissue engineering [54], water remediation for oil and heavy metals [55–58], and concrete self-healing [59–61] or moisture buffering [62]. Alginates are particularly interesting for atmospheric water harvesting because of their inherent affinity with moisture [63,64] and very good biocompatibility [35,43,65].

1.2. Objectives

This research investigates the exploitation of a biopolymer based on alginate for AWH applications. The objective is to define an optimized composition for thermal cycles with regeneration temperatures above 60 °C. The optimization focuses on maximizing the moisture uptake and release kinetics of the sorbent to improve daily water production in low-humidity environments. The final aim is to produce a bioderived polymer capable of running multiple daily cycles of sorption/regeneration to

harvest water from the atmosphere.

2. Methodology

The study consists of three sections. The first section investigates how varying constituent concentrations impact the response of composite biopolymers using calcium alginate to regeneration/sorption cycles. The second section critically analyzes and compares two theories on sorbent kinetics to understand how various parameters affect moisture uptake and to determine the best-fitting modeling approach. The final section describes the optimization strategy based on the developed model to determine an optimal cycling time for low-humidity environments, maximizing moisture uptake capacity and daily water productivity.

2.1. Materials

2.1.1. Synthesis of alginate biopolymer

Calcium alginate (CaAlg) is the basis for producing the different samples of hygroscopic polymers. The polymerization, obtained by crosslinking blocks of Sodium Alginate (NaAlg) hydrogel with Ca²⁺ ions dissolved in a CaCl₂/water solution, exploits the phenomenon called ionotropic gelation [66], generating polymer chains propagated as in the egg-box model [67–70]. NaAlg (repeating blocks of Mannuronate and Guluronate with Na⁺ radical) is a salt originated from the polysaccharide constituents of cell walls from brown algae [71].

Fig. 1 depicts the schematic of the sample synthesis process. Ionotropic gelation is achieved by dripping the NaAlg/water gel into the CaCl₂/water solution, initiating a substitution reaction between Na⁺ and Ca²⁺ upon contact between the interfaces of the two substances. The Na⁺, expelled by the NaAlg monomers, forms a solvated structure with Cl²⁻ residuals in the water solution [66,68,72,73].

Composite hydrogel samples include natural graphite with 99 % carbon and 0.2 % residual ash. Graphite was initially sonicated in demineralized water, obtaining particle sizes between 4–6 µm, and later mixed with the NaAlg hydrogel. The homogeneous viscous gel is dripped into the crosslinking solution containing the Ca²⁺ initiator, instantaneously forming 6–7 mm diameter spherical particles. Then, the spherical beads are thoroughly rinsed with demineralized water and dried in a ventilated oven at 70 °C. Table 1 reports the concentration of each constituent to realize six different compositions labeled from S1 to S6 and the average particle radius over a random selection of 15 spherical particles. The size measurement is the average between the dry (80 °C, RH < 5 %) and wet (30 °C, RH = 55 %) conditions. The salt concentration compared to other referenced [41,43–48] work is 10 times lower to avoid the leak risk and reduce the consumption of materials and waste production.

2.2. Experimental testing

2.2.1. Adsorption/regeneration tests

Initial experimental investigations, conducted on 6 different samples, assessed the influence of each component on the kinetics during sorption and regeneration cycles. These samples (initial weight of approximately 2 g) underwent a preconditioning process in a controlled environment with a fixed temperature and relative humidity (T_{ads} , RH_{ads}) for a duration exceeding 24 h. The preconditioning allowed the samples to establish equilibrium with the surrounding environment. Subsequently, the samples underwent regeneration at a constant temperature (T_{reg}) and ambient vapor pressure using a thermal balance (Kern DBS60-3) with an error of ± 3 mg. The balance monitored samples mass change for the entire duration of the transient fixed at 180 min, sampling one measurement every 5 s. After the regeneration, the samples experienced sorption with the same T_{ads} and RH_{ads} as for the preconditioning. The samples were periodically weighed with an analytical balance (Kern ABJ 320-4NM) with an error of ± 0.3 mg. The weightings

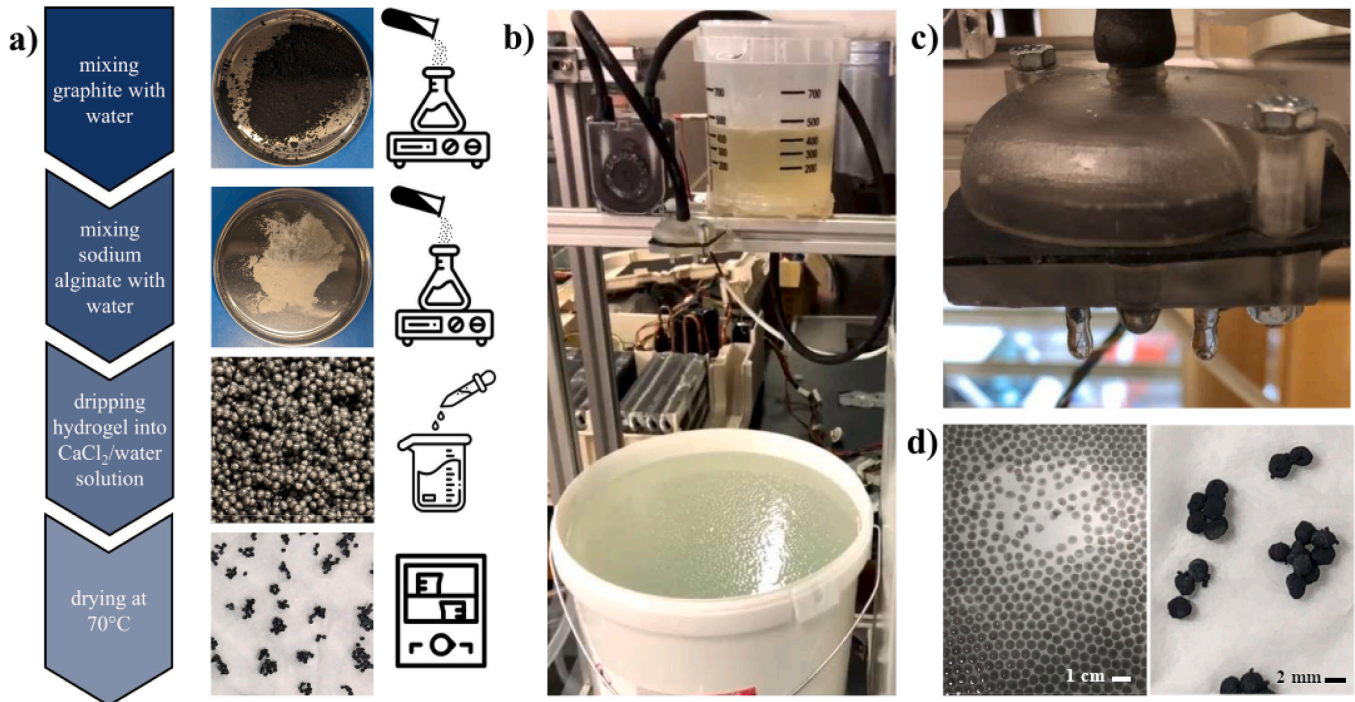


Fig. 1. a) Schematization of the procedure for realizing spherical particles based on Calcium Alginate. b) A picture of the setup dripping the composite hydrogel in the crosslinking bath with calcium chloride. c) Magnification of the 3D-printed nozzle to drip the hydrogel. d) Spherical particles of crosslinked calcium alginate with graphite formed after the dripping of the hydrogel into the CaCl₂/water solution. The picture on the right highlights that upon drying at 70 °C in a ventilated oven, the final shape of the particle considerably shrank compared to its original form.

Table 1

Sample list with concentrations of each component used for the biopolymer synthesis and sample average particle radius. Each column reports the water mass ratio of NaAlg, CaCl₂, and graphite used for the preparation.

	S1	S2	S3	S4	S5	S6
NaAlg/H ₂ O [%]	1	1	2	2	1	1
CaCl ₂ /H ₂ O [%]	5	10	5	10	5	5
Graphite/H ₂ O [%]	0	0	0	0	0.1	0.025
Particle radius (mm)	0.65	0.68	0.59	0.68	0.91	0.68
Label	Alg ₁ Ca ₅	Alg ₁ Ca ₁₀	Alg ₂ Ca ₅	Alg ₂ Ca ₁₀	Alg ₁ Ca ₅ G _{0.1}	Alg ₁ Ca ₅ G _{0.025}

were: 6 times every 10 min for the first hour, 8 times every 15 min, and 4 times every 30 min. This comprehensive measurement schedule covered 3 h of the regeneration process and 5 h of the sorption process. The procedure was repeated for each sample, with a constant T_{ads} of 21 °C. However, the RH_{ads} were adjusted to achieve equivalent environments at 30% and 50% during preconditioning. Similarly, tested regeneration temperature was 60 °C, 80 °C and 100 °C. The results of these tests are presented and discussed in Figs. 2 and 3.

2.2.2. Scanning electron microscopy

After completely drying at 100 °C, samples S1 (with no graphite) and S5 (with a graphite/water ratio of 0.1 %) are imaged using Scanning Electron Microscopy (SEM) (FEI Quanta). Fig. 4 reports two magnifications outlining the main differences on the outer surface generated by adding graphite to the biopolymer.

2.3. Theoretical models

The study exploits two distinct model families to describe moisture mass transfer: Fick's law of diffusion (FD) [18,74,75] and Linear Driving Force (LDF) [18,74,76] potential. The FD models involve mathematical expressions derived from the integration of Fick's first and second laws of diffusion. On the other hand, the LDF models encompass different modifications of the Newtonian simplification of Linear Driving Force

potential.

Both the FD models and the LDF models establish a relationship between the average concentration (C^- [kgH₂O/m³]) across the volume of the sorbent and time. On the other hand, experiments provide information in terms of water uptake $w(t)$, i.e., the instantaneous mass of water per unit of sorbent dry mass [gH₂O/g_{dry-sorbent}]). Under the hypothesis of sorbent constant volume during both adsorption/desorption processes, the fractional approach to equilibrium $\varepsilon(t)$ in Eq. (1) provides the link between C^- and $w(t)$, for each time of the transformation [18,74,77]. Subscripts “0” and “eq” represent the initial and equilibrium quantities.

$$\varepsilon(t) = \frac{\bar{C}(t) - C_0}{C_{eq} - C_0} = \frac{w(t) - w_0}{w_{eq} - w_0} \quad (1)$$

In addition, the engineering applications and experimental tests focus on the average adsorbate (C^-) at each time rather than its spatial distribution (C). The link between the two terms for a spherical particle, p , is given by:

$$\bar{C}(t) = \frac{1}{V_p} \int_{V_p} C(r, t) \cdot dV \quad (2)$$

2.3.1. Fick's law of diffusion

The mass rate of water vapor diffusion per unit area of the sorbent (J

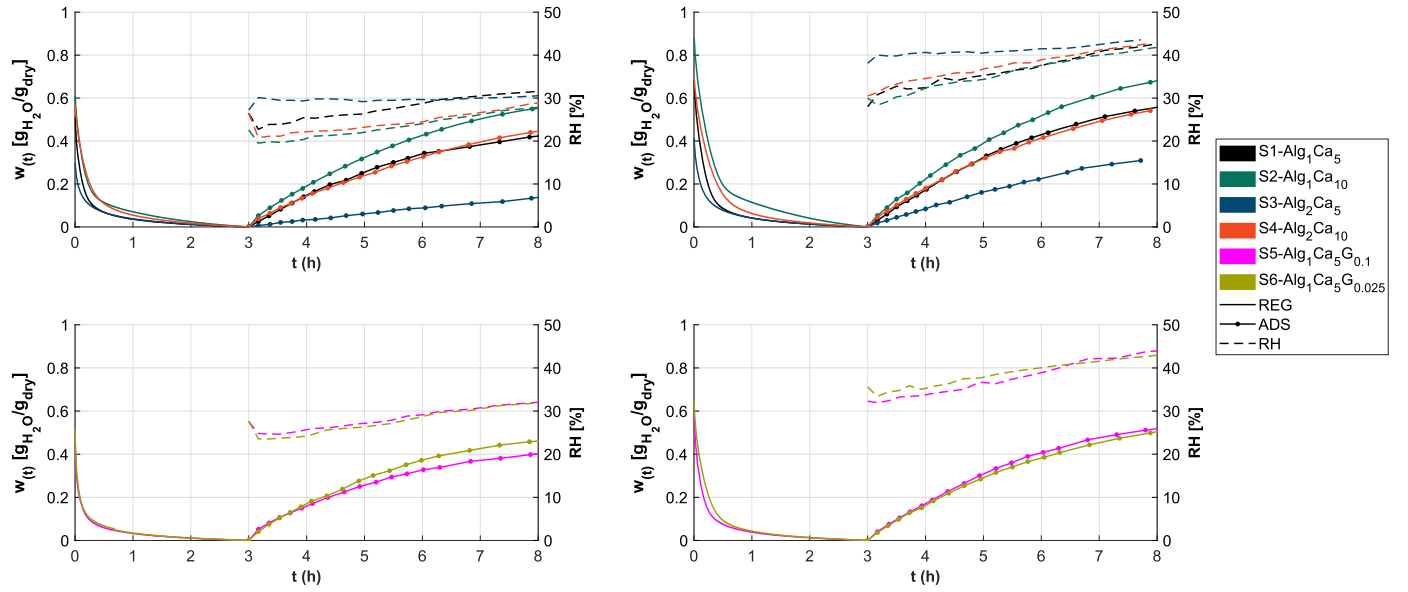


Fig. 2. Time-dependent water uptake variation between sorption and regeneration. On the x-axis, the time t in hours; on the left y-axis, the water uptake $w(t)$; on the right y-axis, the relative humidity RH within the conditioning chamber during sorption. a) Results of samples S1, S2, S3, S4 at low humidity. b) Results S1, S2, S3, and S4 at medium humidity. c) Results of samples S5 and S6 at low humidity. d) Results of samples S5 and S6 at medium humidity.

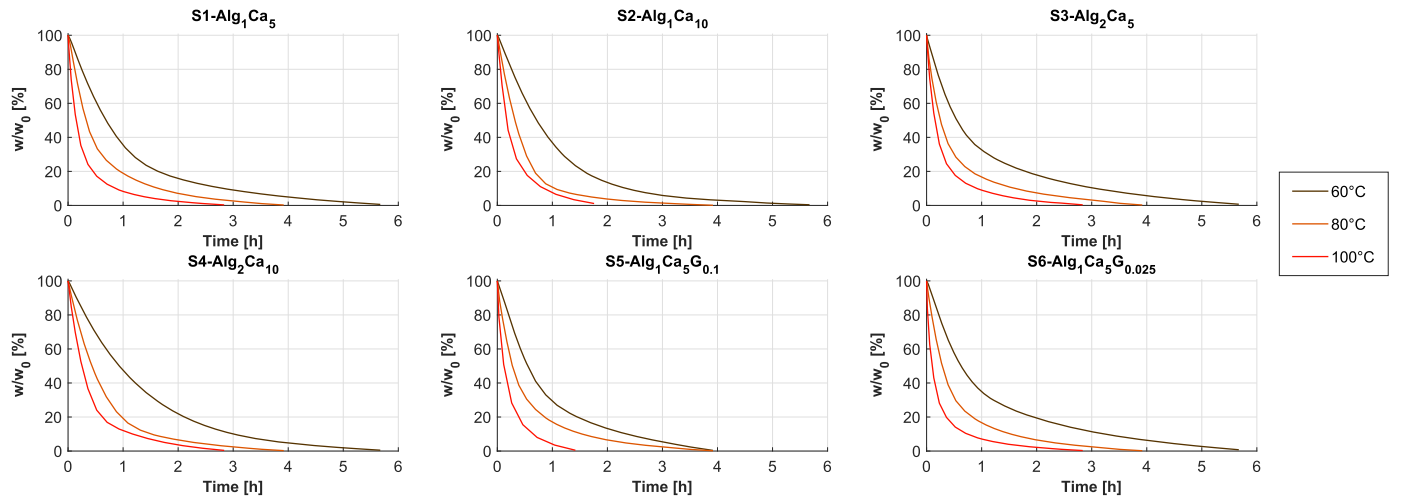


Fig. 3. Effect of regeneration temperature on desorption kinetics for each tested composition. In the y-axis, the water uptake normalized to the equilibrium value.

[kg/m²s]) is proportional to the normal (n) gradient of water concentration (C [kg/m³]) as in Eq. (3)[74]. The diffusivity D [m²/s] is the coefficient of proportionality linking the flux with the normal concentration gradient. The mass balance around a non-deformable elementary volume of interest by J describes the variation of C over time as in Eq. (4).

$$J = -D \frac{\partial C}{\partial n} \quad (3)$$

$$\frac{\partial C}{\partial t} = \nabla \cdot (D \nabla C) \quad (4)$$

Under the hypotheses listed below, Eq. (4) transforms into Eq. (5).

- i) Independence of diffusivity by space coordinates and directions (i.e., homogeneous and isotropic material).
- ii) Physical and geometrical spherical symmetry (the sorbent is a spherical particle with radius r).

- iii) Differently from typical solid sorbent particles, i.e., obtained by the aggregation of single sorbent crystals, thus generating intracrystalline macro-porosity, the crosslinking process producing CaAlg biopolymers generated directly single spherical particle, equivalent to a unique single sorbent crystal. Thus, the typical corrective coefficient for macro-porosity ($\epsilon_p^{18,82}$) is negligible. Diffusive resistance relates only to micro-porosity;
- iv) The heat related to adsorption/desorption does not influence the temperature of particles or the chamber. Hence, processes follow an isothermal transformation.
- v) Dependency of D from instantaneous water uptake is negligible. Thus, D is a constant over the time domain.

$$\frac{\partial C}{\partial t} = D \cdot \left(\frac{\partial^2 C}{\partial r^2} + \frac{2}{r} \frac{\partial C}{\partial r} \right) \quad (5)$$

The spatial integration domain is between the center ($r = 0$) and the particle radius ($r = R_p$). The physical conditions at these two boundaries must be coherent with testing conditions to obtain proper results. Thus, their correct choice leads to analytical solutions for Eq. (5).

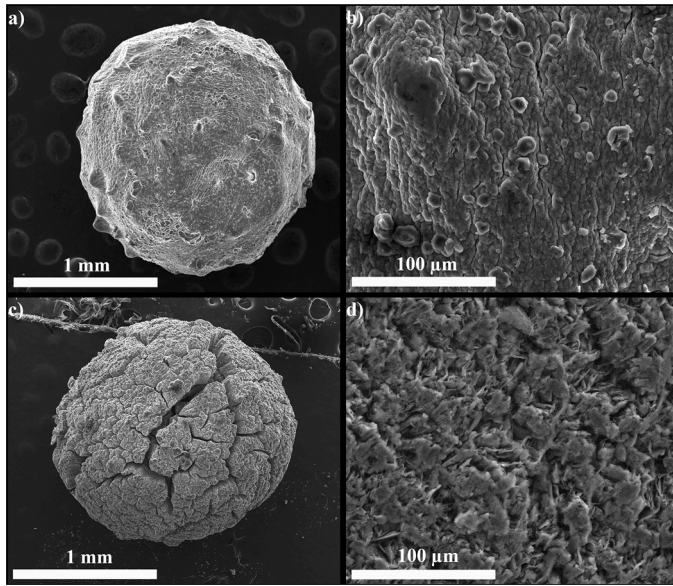


Fig. 4. SEM imaging of two spherical beads of CaAlg biopolymer. a) Spherical particle with the S1 composition. b) zoom of its outer surface. c) Spherical particle with 0.025 % (sample S6) graphite concentration composition. d) zoom of its outer surface.

The first boundary is $C(r = R_p) = C_\infty \forall t$. Indeed, knowing that water diffusivity in sorbents is many orders of magnitude lower than water diffusivity in the air (i.e., at ambient temperature $D_{H_2O-air} \sim 2.4 \times 10^{-5} \text{ m}^2/\text{s}$ [18] while for silica gel $D_{H_2O-(SiO_2)_n} \sim 10^{-11} \text{ m}^2/\text{s}$ [18,81,82]), the water vapor boundary layer around the particle can be neglected. Hence, the particle's outer surface ($r = R_p$) immediately reaches air bulk conditions, i.e., the conditions of the undisturbed environment at any moment. Given the isothermal hypothesis, this equilibrium equals the sorbent-moisture adsorption isotherm (C_{eq}). Then the equivalence $C(r = R_p) = C_\infty = C_{eq}$ is valid.

Table 2

Analytical solutions of Fick's diffusion considering first a constant humidity condition at the boundary layer (FD), second a linear variation of humidity at the boundary layer (FD_{RH}); third, a stepwise instantaneous equilibrium within the sorbent particle, under the hypothesis of a linear variation of RH (FD_{SW}).

Model	Additional hypotheses	I.C. and B.C.	Analytical Solution
FD[74] Constant humidity FD	- C_∞ constant over time	$\begin{cases} C _{r,t=0} = C_0 \\ C _{r=R_p,t} = C_\infty \\ \frac{\partial C}{\partial r} _{r=0} = 0 \end{cases}$	$\varepsilon(t) = 1 - \frac{6}{\pi^2} \sum_{n=1}^{\infty} \left[\frac{e^{-\pi^2 n^2 \left(\frac{D \cdot t}{R_p^2} \right)}}{n^2} \right] \quad (6)$
FD _{RH} Linearly variable humidity FD	<ul style="list-style-type: none"> - C_∞ is a time-dependent function - $C_\infty(t)$ is a function proportional to ambient air $RH(t)$ - $RH(t)$ changes linearly between RH_i at time $t_i=0$ and RH_f at time t_f - initial sorbent concentration is null 	$\begin{cases} C _{r,t=0} = 0 \\ C _{r=R_p,t} = C_\infty(t) \\ \frac{\partial C}{\partial r} _{r=0} = 0 \end{cases}$	$\varepsilon(t)_{C_0, w_0=0} = \left(\frac{6D}{R_p^2} \right) \cdot \sum_{n=1}^{\infty} \left[e^{-\pi^2 n^2 \left(\frac{D \cdot t}{R_p^2} \right)} \cdot \int_0^t (p + q \cdot \tau) \cdot e^{\pi^2 n^2 \left(\frac{D \cdot \tau}{R_p^2} \right)} d\tau \right] =$ $\dots = \left(\frac{6D}{R_p^2} \right) \cdot \sum_{n=1}^{\infty} \left\{ \frac{p + qt}{K \cdot n^2} - \frac{q}{(K \cdot n^2)^2} + \left[\frac{q}{(K \cdot n^2)^2} - \frac{p}{K \cdot n^2} \right] \cdot e^{-K \cdot n^2 \cdot t} \right\} \quad (7)$ <p>where</p> $\begin{cases} p = \frac{1}{RH_{eq}} \left[RH_i - \left(\frac{RH_f - RH_i}{t_f - t_i} \right) \cdot t_i \right] \\ q = \frac{1}{RH_{eq}} \cdot \left(\frac{RH_f - RH_i}{t_f - t_i} \right) \\ K = \frac{\pi^2 \cdot D}{R_p^2} \end{cases} \quad (8)$
FD _{SW} Stepwise FD	<ul style="list-style-type: none"> - $C_\infty(t)$ varies as in FD_{RH} - the particle reaches a uniform concentration within each finite integrating time step $t_j < t < t_{j+1}$ 	$\forall j^{\text{th}} \text{ time interval } t \in t_j < t < t_{j+1}:$ $\begin{cases} C _{r,t=t_j} = C_j \\ C _{r=R_p,t} = C_\infty(t_j) \\ \frac{\partial C}{\partial r} _{r=0} = 0 \end{cases}$	$\forall j^{\text{th}} \text{ time interval } t \in t_j < t < t_{j+1}:$ $\varepsilon(t)_j = \frac{\bar{C}(t) - C_j}{C_\infty(t_j) - C_j} = \frac{w(t) - w_{0j}}{w_{eq}(t_j) - w_{0j}} = 1 - \frac{6}{\pi^2} \sum_{n=1}^{\infty} \left[\frac{e^{-\pi^2 n^2 \left(\frac{D \cdot (t - t_j)}{R_p^2} \right)}}{n^2} \right] \quad (9)$

The second boundary results from the spherical symmetry: $\partial C / \partial r|_{r=0} = 0$ (the mass flux at the center of the spherical particle is null).

Table 2 summarizes three different analytical solutions (FD, FD_{RH}, FD_{SW}) obtained by integrating Eq. (5), in combination with Eqs. (1) and (2), according to each specific boundary (B.C.) and initial conditions (I.C.).

The FD represents the typical solution when relative humidity at the boundary layer is constant over the moisture transfer transient [74].

The first proposed alternative, FD_{RH} (analytical passages in section A5 of supplementary information), results from the analytical integration considering linear time dependant concentration of water vapor in the air, as the equation $C_\infty(t) = p + qt$ such that $C_\infty(t) = C_{\infty,eq} RH(t) / RH_{eq}$. This solution is suitable only for adsorption since the initial concentration must be null.

The second alternative model, FD_{SW}, is a step-wise variant of the FD model with constant air humidity. The solution comes from the subdivision of the entire time interval, t , into subintervals of small and finite duration $t_j < t < t_{j+1}$. The initial concentration of each subinterval is assumed to be uniform and equal to the equilibrium concentration of the previous subinterval. This approximation assumes a uniform concentration all over the spherical particle. In reality, this condition is hard to achieve, and the resulting implications are discussed in the following sections.

2.3.2. Linear driving force potential

The LDF model follows a Newtonian analogy for defining the sorption driving force. In particular, the mass transfer crossing the sorbent outer surface is proportional to the difference between the instantaneous gas-side bulk concentration C_∞ and the average adsorbate concentration $\bar{C}(t)$.

$$\frac{d\bar{C}(t)}{dt} = K \cdot [C_\infty(t) - \bar{C}(t)] \quad (10)$$

As shown in Eq. (11), the proportionality factor, K , includes the sorbent effective diffusivity (D), the square of the particle radius, and a shape factor (F_0). In the case of spherical particles and average concentration defined as in Eq. (2), F_0 equals to 15 is a typical excess

approximation⁸¹:

$$K = \frac{F_0 \cdot D}{R_p^2} \quad (11)$$

The hypotheses listed before, from *i*) to *iv*), are still valid under the LDF model. Table 3 summarizes three different analytical solutions (LDF, LDF_{DW}, LDF_m) obtained by integrating Eq. (10) in combination with Eq. (1) according to each specific boundary (B.C.) and initial conditions (I.C.).

The base LDF solution follows the integration of Eq. (10) under the additional hypothesis and the specific initial condition (I.C.), as reported in Table 3.

The LDF_{DW} model (analytical passages in section A6 of supplementary information) supposes a dependency of diffusivity by the adsorbate concentration, keeping C_{∞} and R_p constant. In particular, the dependence is supposed to be linear, where the dependent variable is the instantaneous water uptake: $D(w_{(t)}) = a + b w_{(t)}$. The time integration provides an analytical solution dependent on the two parameters, a and b , keeping a physical interpretation of the others.

On the contrary, the LDF_m⁸³ model includes a corrective parameter m as an exponent of the adimensional group $(D t / R_p^2)$ [78]. The coefficient introduces additional freedom, improving the successive fitting procedure. On the other hand, the physical interpretation of the model is less strict.

2.4. Fitting procedures for the evaluation of diffusivity

Validation of the analytical solutions reported in Tables 2 and 3 follows a fitting procedure against experimental tests performed for each sample and for each testing condition, i.e., RH_{ads} (30 %, 50 %), T_{ads} (21 °C), and T_{reg} (60 °C, 80 °C, 100 °C). The fitting procedure goal is quantifying D with the different hypotheses and models.

The fitting procedure follows the criteria of the least square root error minimization [79]. It consists of searching, for each of the analytical solutions, the values of the parameters minimizing the error function $err(p_1, p_2, \dots, p_M)$ as defined in Eq. (15). It is the total sum of the squared differences between each experimental value y_i and the model value $f(t_i, p_1, \dots, p_M)$, evaluated at the same time t_i .

$$err(p_1, p_2, \dots, p_M) = \sum_{i=1}^N [f(t_i, p_1, p_2, \dots, p_M) - y_i]^2 \quad (15)$$

The function $f(t_i, p_1, p_2, \dots, p_M)$ is the instantaneous water uptake $w_{(t)}$. The algorithm used for the error function minimization is the Simplex Nelder-Mead method [80,81]. The residual tolerance truncating the optimization algorithm is 10^{-14} in all tested models.

Table 4 lists the error function parameters and their initialization value for the adsorption and regeneration phases. For FD_{SW} the number of sub-intervals is 100, while the time tessellation is composed of a grid of 200 nodes.

Table 3

Analytical solutions of the linear driving force model considering first constant diffusivity against the water uptake (LDF); second, a linear dependence of diffusivity from water uptake (LDF_{DW}); third, a coefficient m affecting the adimensional exponent of the solution (LDF_m).

Model	Additional hypotheses	I.C.	Analytical Solution
LDF[18] Baseline	- hypothesis v) is valid	$\bar{C}(t=0) = C_0$	$\varepsilon(t) = 1 - e^{-\frac{F_0 \cdot D}{R_p^2} t} \quad (12)$
LDF _{DW} w dependent diffusivity LDF	- hypothesis v) is modified. D is linearly dependent on water uptake as follows: $D(w) = a + b \cdot w(t)$	$\bar{C}(t=0) = C_0$	$\varepsilon(t) = \frac{e^{-\frac{F_0(a+b w_{eq})}{R_p^2} t} - 1}{e^{-\frac{F_0(a+b w_{eq})}{R_p^2} t} + b \cdot \left(\frac{w_{eq} - w_0}{a + b w_0}\right)} \quad (13)$
LDF _m ⁸³ Modified LDF	- hypothesis v) is valid - a corrective power coefficient m is introduced	$\bar{C}(t=0) = C_0$	$\varepsilon(t) = 1 - e^{-F_0 \cdot \left(\frac{D}{R_p^2} t\right)^m} \quad (14)$

Table 4

Parameters used for the fitting procedure through the minimization method based on the Nelder-Mead algorithm.

Equation parameters	Analytical solution					
	FD	FD _{RH}	FD _{SW}	LDF	LDF _{DW}	LDF _m
M	$M = 1$	$M = 1$	$M = 1$	$M = 1$	$M = 2$	$M = 2$
p_1	$p_1 = D$	$p_1 = D$	$p_1 = D$	$p_1 = D$	$p_1 = a$	$p_1 = D$
p_2					$p_2 = b$	$p_2 = m$
D	$D_{init} = 10^{-12} \text{ m}^2/\text{s}$				$a_{init} = b_{init} = 10^{-12} \text{ m}^2/\text{s}$	$D_{init} = 10^{-12} \text{ m}^2/\text{s}$
D_{init}						$m_{init} = 1$
D_{init}	$D_{init} = 5 \times 10^{-11} \text{ m}^2/\text{s}$				$a_{init} = b_{init} = 5 \times 10^{-11} \text{ m}^2/\text{s}$	$D_{init} = 5 \times 10^{-11} \text{ m}^2/\text{s}$
m_{init}						$m_{init} = 1$

3. Results and discussion

3.1. Influence of CaCl_2 , NaAlg , and graphite on sorption/regeneration kinetics

Fig. 2 presents the water uptake variations of each sample during the regeneration and sorption cycles at two different relative humidity (RH) levels, 30 % and 50 %. Fig. 2a and b correspond to samples S1, S2, S3, and S4 (without graphite), while Fig. 2c and d represent samples S5 and S6 (with graphite). The solid lines in the graphs, depicted on the left vertical axis, represent the changes in water uptake throughout the regeneration phase (first 3 h) and the subsequent sorption phase (last 5 h). On the other hand, the dotted lines illustrate the RH values measured within the chamber during the sorption phase. During the regeneration phase, there is no humidity control, and samples experience ambient vapor pressure conditions at the specified regeneration temperature.

Higher RH shifts the sorption uptake curves towards higher values, increasing the equilibrium water uptake and the initial slope of $w_{(t)}$. The equilibrium value w_{eq} is the intercept value at the time 0, hence the w_0 of the regeneration phase. It results from the exposure of samples for more than 24 h within the conditioning chambers.

The RH in the chamber with controlled humidity increases over time, starting from an initial RH_0 close to 25 % and increasing towards the equilibrium value of 30 %. RH_0 is close to 30 % in the second case, while the final value is around 42 %, still far from the equilibrium value of 50 %. Right after the end of the regeneration, the sample is positioned in the chamber with an RH equal to RH_{eq} . The moisture sorption rate is high when the material is completely dry, influencing the chamber RH . The influence reduces over time as the $w_{(t)}$ of the sample increases and the water mass rate decreases.

For this reason, during the experiment, samples experienced an average humidity condition (RH_{avg}) lower than the RH_{eq} designed for the experiment itself. Table 5 reports actual values related to water uptakes

Table 5

The table reports values of regeneration/sorption tests: the water uptake at the start of regeneration (w_0 , coincident with equilibrium water uptake at the specified RH and $T = 21^\circ\text{C}$); the water uptake after 5 h of sorption (w_{5h}); RH at the start (RH_0) and end (RH_{5h}) of sorption, and the average RH_{avg} .

Sample label	RH = 20–34 %					RH = 30–47 %				
	w_0 [gH ₂ O/gdry]	w_{5h} [gH ₂ O/gdry]	RH_0 [%]	RH_{5h} [%]	RH_{avg} [%]	w_0 [gH ₂ O/gdry]	w_{5h} [gH ₂ O/gdry]	RH_0 [%]	RH_{5h} [%]	RH_{avg} [%]
S1	0.515	0.436	26.46	33.44	27.17	0.683	0.562	28.00	48.10	35.35
S2	0.610	0.570	22.57	34.40	22.90	0.880	0.706	30.00	46.20	34.95
S3	0.300	0.149	27.23	33.95	29.63	0.412	0.309	38.10	48.40	40.82
S4	0.573	0.464	26.43	33.82	24.04	0.695	0.542	30.50	47.52	36.47
S5	0.448	0.407	27.55	33.58	27.76	0.601	0.527	32.30	46.00	36.87
S6	0.518	0.468	27.71	34.62	27.06	0.647	0.522	35.60	45.87	38.11

and RH experienced by each sample and for each testing condition. The increased CaCl_2 concentration, i.e., evident by comparing sample S2 with S1 or S4 with S3, increases the material sorption capacity and the slope of $w(t)$. On the other hand, increasing NaAlg content but keeping constant the CaCl_2 concentration lowers the sorption performances (comparing S1 with S3 and S2 with S4).

Despite CaCl_2 concentration being 5–10 %, this study achieved water uptake levels between 0.6–0.9 g/g under vapor pressures of 0.6–1.2 kPa. These results outperform most referenced compositions, although salt concentrations are close to the saturation level (30–46% wt) [30,31,25, 41–43,47,48,34,32,2,35–37,33,38,39]. Three configurations with high salt content reported better equilibrium results. The first configuration involved PAM polymer [40] with an impregnation of LiCl exceeding 40% wt. The resulting equilibrium uptake is 1.5 g/g at 30% RH and 25°C . In the second one, impregnation of CNF[24] occurs in two consecutive stages: with MgSO_4 (10% wt) and LiCl (46% wt). This binary-salt configuration achieved a 1.7 g/g water uptake at 45 % RH and 20°C . The third configuration utilized a similar double-stage impregnation process with an alginate-based hydrogel [44]. First, with LiCl (46% wt) and then with CaCl_2 (43% wt), obtaining a binary-salt configuration with 1.3 g/g water uptake at 20% RH and 25°C .

However, only one configuration achieved higher equilibrium uptake with low salt content. This configuration involved a vertically aligned porous matrix of GO-alginate hydrogel [45] impregnated with 10 % wt LiCl, resulting in a 1.5 g/g water uptake at 30 % RH and 30°C . Directional freezing of samples with liquid nitrogen created vertical ice pillars that, once transformed into empty pores with vacuum drying, generated the aligned porous matrix. This process induces a significant level of microporosity, reducing material density and volumetric uptake.

The addition of graphite has a positive influence on sorption capacity. At lower RH, sample S5 reaches higher values and is faster than sample S1 or S3 (with equivalent content of CaCl_2). On the other hand, increasing the graphite concentration (S6 versus S5) leads to performance deterioration. Most probably, given the coarse dimension of graphite flakes within the composition, the increase in concentration might lead to pore occlusion. This evidence suggests the presence of a trade-off between graphite concentration with a specific particle dimension requiring optimization. The influence of graphite content is especially evident in the case of low RH. In contrast, at higher RH, the increase in graphite concentration has a less negative influence on capacity and kinetics.

Fig. 3 shows the temperature effects on the desorption kinetics of the samples. In all test cases, the increase of NaAlg from 1 % to 2 % does not generate evident influences on the regeneration kinetics. On the other hand, the increase of CaCl_2 has an evident influence on the regeneration test at 80°C . It increases the initial slope of the curves, reducing the differences with the 100°C regeneration temperature.

The addition of graphite has a more evident influence on regeneration. Indeed, high graphite content speeds up regeneration kinetics for all tested temperatures 60, 80, and 100°C . Further on, the rapidity of reduction of $w(t)$ at 80°C is higher.

3.2. Influence of graphite on material structure

As shown in Fig. 4, the SEM images reveal the structural effects of graphite addition to the CaAlg biopolymer. The addition of graphite results in higher surface roughness of the particles. The introduction of graphite particles generates irregularities that can impact surface adhesion and wettability. Furthermore, the figure evidences the layered crystalline structure of graphite on the surface of the particles. SEM images support the fact that graphite particles play a role in the structural organization of the hydrogel network, thus affecting properties such as overall porosity, pores size distribution, permeability, diffusivity, and the consequent transport of molecules within the composite material. The modification of these properties may be influenced by the concentration and size of the graphite particles, as indicated by the results in Section 3.1.

The presence of cracks on the surface of the particles suggests that the incorporation of graphite alters the drying process of the hydrogel composite. These modifications can impact mechanical strength and fatigue. However, the quantification of these properties requires further studies.

3.3. Models validation

3.3.1. FD and LDF validation against experimental results

Fig. 5 displays the results of the fitting procedure outlined in Section 2.4. Fig. 5a and b compare the experimental results of regeneration/sorption tests with the fitting models based on Fick Diffusion (FD , FD_{RH} , FD_{SW}) and their absolute error (difference between fitting and experimental values). The bottom graphs provide the same comparison for the Linear Driving Force (LDF , LDF_{Dw} , LDF_m) models. This figure specifically pertains to sample S1, tested at 47 %. Supplementary information in sections A1 and A2 includes the same results for the remaining sample and testing conditions.

All the models demonstrate good agreement with the regeneration and sorption results. The FD and FD_{RH} models exhibit the highest absolute error, with an underestimation of approximately 0.1 g/g during the first 2 h. Among the FD models, FD_{SW} provides the best approximation of the sorption results (maximum absolute error around 0.02 g/g). However, it generates larger errors in the approximation of regeneration.

The FD and FD_{RH} models show a steeper slope during the initial sorption steps. In contrast, the FD_{SW} model, due to the imposed equilibrium within the simulation timestep, aligns better with experimental data. However, such a result implies a less straightforward physical interpretation of the data. The FD_{SW} approximation generates discrepancies in diffusivity coefficients resulting from the fitting process, as reported in Table 6 for sorption and regeneration. The FD and FD_{RH} models yield similar D values in the order of $10^{-11} \text{ m}^2/\text{s}$ and $10^{-12} \text{ m}^2/\text{s}$ for regeneration and sorption, respectively; on the other hand, the FD_{SW} provides values in the order of $10^{-12} \text{ m}^2/\text{s}$ and $10^{-13} \text{ m}^2/\text{s}$ for regeneration and sorption, respectively.

The variation in RH does not significantly impact the D values. Thus,

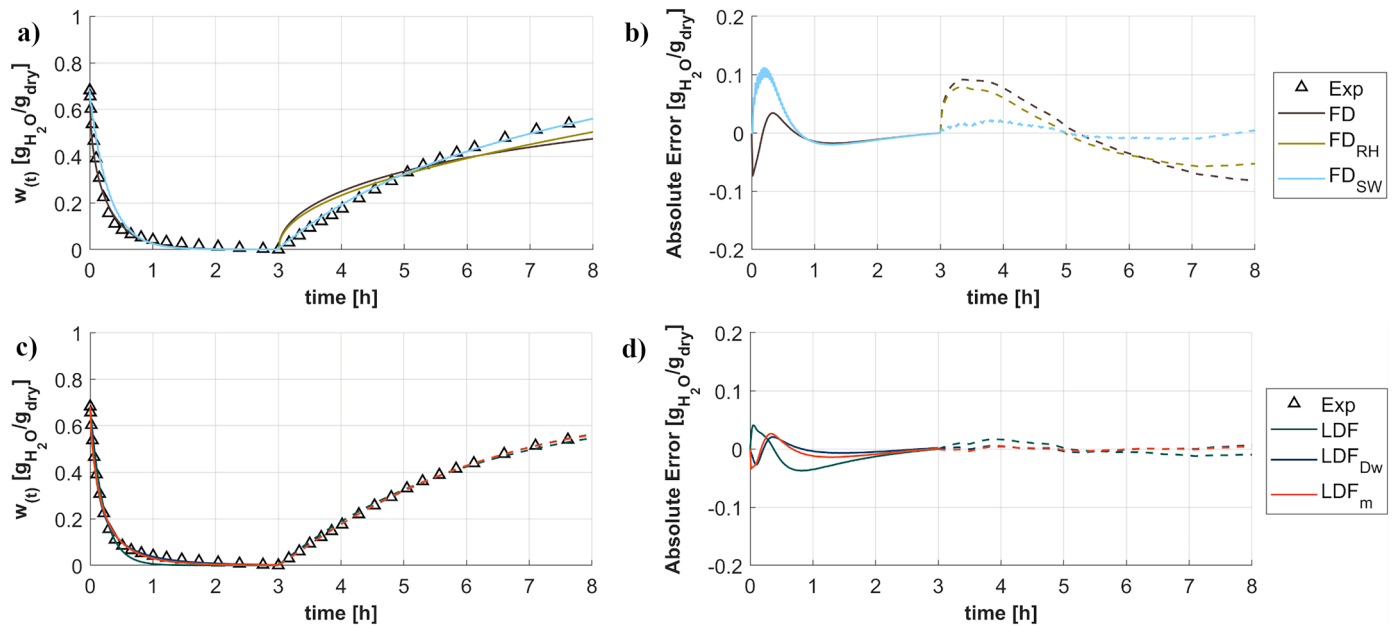


Fig. 5. a) Comparison between the experimental values of the regeneration/sorption test of sample S1 at 47 % and the values obtained from models FD, FD_{RH}, and FD_{SW}, using the optimization method of paragraph 2.4. b) The absolute error with respect to experimental data generated with each model and at each time. c) and d) report the same information for the models LDF, LDF_{Dw}, and LDF_m.

Table 6

Diffusion coefficients resulting from the fitting procedure of FD-derived models on each regeneration and sorption.

RH _{avg}	D _{REG} [m ² /s]				D _{ADS} [m ² /s]					
	20–30 %		30–40 %		20–30 %		30–40 %			
Model	FD	FD _{SW}	FD	FD _{SW}	FD	FD _{RH}	FD _{SW}	FD	FD _{RH}	FD _{SW}
S1	3.66E ⁻¹¹	8.75E ⁻¹²	3.27E ⁻¹¹	6.34E ⁻¹²	1.95E ⁻¹²	2.97E ⁻¹²	2.00E ⁻¹³	1.72E ⁻¹²	4.49E ⁻¹²	2.76E ⁻¹³
S2	2.65E ⁻¹¹	4.53E ⁻¹²	2.04E ⁻¹¹	2.43E ⁻¹²	2.62E ⁻¹²	6.55E ⁻¹²	3.43E ⁻¹³	1.71E ⁻¹²	3.64E ⁻¹²	2.17E ⁻¹³
S3	1.82E ⁻¹¹	2.72E ⁻¹²	2.19E ⁻¹¹	3.91E ⁻¹²	2.89E ⁻¹³	4.28E ⁻¹³	1.53E ⁻¹⁴	1.01E ⁻¹²	1.59E ⁻¹²	7.30E ⁻¹⁴
S4	2.61E ⁻¹¹	3.89E ⁻¹²	2.32E ⁻¹¹	2.84E ⁻¹²	1.62E ⁻¹²	2.74E ⁻¹²	1.21E ⁻¹³	1.71E ⁻¹²	3.73E ⁻¹²	1.98E ⁻¹³
S5	8.14E ⁻¹¹	2.38E ⁻¹¹	7.45E ⁻¹¹	1.78E ⁻¹¹	5.35E ⁻¹²	7.81E ⁻¹²	6.27E ⁻¹³	4.24E ⁻¹²	7.80E ⁻¹²	6.09E ⁻¹³
S6	4.87E ⁻¹¹	1.59E ⁻¹¹	3.20E ⁻¹¹	5.60E ⁻¹²	2.69E ⁻¹²	4.20E ⁻¹²	3.02E ⁻¹³	1.72E ⁻¹²	2.70E ⁻¹²	1.62E ⁻¹³

the increase in the slope of $w(t)$ is explained by the rise in the equilibrium potential rather than the change in diffusivity. In contrast, during all regeneration processes, the D value is one order of magnitude higher than in sorption, suggesting a significant influence of temperature.

The simple LDF model is in better agreement than the FD-based models in regeneration and sorption, with a maximum absolute error on water uptake below 0.05 g/g. The approximation further improves when the number of freedom degrees increases to two, as with LDF_m and LDF_{Dw} models. While for LDF and all the FD models, the largest errors were restricted to the first 40 min of regeneration.

The superior agreement of LDF-based models compared to FD variants is likely attributed to the assumption of constant particle volume and the independence of D from concentration. This polymer-based

sorbent exhibits larger uptake variations (between 0 and 0.8–0.9 g/g) and demonstrates visible swelling behavior between the dry and wet states.

Table 7 presents the D values for all the LDF-based models. Table 8 provides the values of parameters a and b for the linear function $D(w) = a + b \cdot w(t)$ for LDF_{Dw} and the exponent m for the LDF_m model.

All the LDF models yield D values close to those of FD and FD_{RH}, indicating consistency among the different simulation approaches. Although LDF_m, due to its nature, has a less strict physical interpretation (especially when m is far from 1, as it happens with regeneration), it can be concluded that temperature is the main factor contributing to error generation. The subsequent paragraph delves into a detailed discussion of the role of temperature on diffusivity and its relationship with water

Table 7

Diffusion coefficients resulting from the fitting procedure of LDF-derived models on each regeneration and sorption.

RH _{avg}	D _{REG} [m ² /s]						D _{ADS} [m ² /s]					
	20–30 %			30–40 %			20–30 %			30–40 %		
Model	LDF	LDF _{Dw}	LDF _m	LDF	LDF _{Dw}	LDF _m	LDF	LDF _{Dw}	LDF _m	LDF	LDF _{Dw}	LDF _m
S1	4.38E ⁻¹¹	8.71E ⁻¹¹	6.27E ⁻¹²	3.68E ⁻¹¹	4.93E ⁻¹¹	1.29E ⁻¹¹	2.71E ⁻¹²	2.93E ⁻¹²	2.97E ⁻¹²	2.54E ⁻¹²	2.97E ⁻¹²	3.24E ⁻¹²
S2	3.21E ⁻¹¹	5.42E ⁻¹¹	4.80E ⁻¹²	2.32E ⁻¹¹	2.59E ⁻¹¹	7.36E ⁻¹²	3.40E ⁻¹²	4.08E ⁻¹²	4.22E ⁻¹²	2.53E ⁻¹²	2.55E ⁻¹²	2.56E ⁻¹²
S3	2.16E ⁻¹¹	7.78E ⁻¹¹	2.66E ⁻¹²	2.61E ⁻¹¹	6.62E ⁻¹¹	3.58E ⁻¹²	7.67E ⁻¹³	1.25E ⁻¹²	9.04E ⁻¹³	1.71E ⁻¹²	3.02E ⁻¹²	2.61E ⁻¹²
S4	2.97E ⁻¹¹	4.78E ⁻¹¹	8.34E ⁻¹²	2.52E ⁻¹¹	3.02E ⁻¹¹	1.32E ⁻¹¹	2.45E ⁻¹²	2.70E ⁻¹²	2.61E ⁻¹²	2.62E ⁻¹²	2.62E ⁻¹²	2.58E ⁻¹²
S5	1.03E ⁻¹⁰	2.53E ⁻¹⁰	6.93E ⁻¹²	8.78E ⁻¹¹	1.49E ⁻¹⁰	1.42E ⁻¹¹	6.78E ⁻¹²	6.07E ⁻¹²	5.86E ⁻¹²	5.72E ⁻¹²	6.84E ⁻¹²	7.13E ⁻¹²
S6	6.29E ⁻¹¹	1.35E ⁻¹⁰	3.40E ⁻¹²	3.58E ⁻¹¹	5.05E ⁻¹¹	1.18E ⁻¹¹	3.50E ⁻¹²	4.04E ⁻¹²	3.96E ⁻¹²	2.54E ⁻¹²	2.59E ⁻¹²	2.58E ⁻¹²

Table 8

Values of coefficients a and b of the equation $D(w) = a + b \cdot w(t)$ for the model LDF_{DW} , and values of coefficients m for the model LDF_m .

RH _{avg}	Regeneration						Sorption					
	20–30 %			30–40 %			20–30 %			30–40 %		
	a [m ² /s]	b [m ² /s]	m	a [m ² /s]	b [m ² /s]	m	a [m ² /s]	b [m ² /s]	m	a [m ² /s]	b [m ² /s]	m
S1	4.27E ⁻¹²	1.66E ⁻¹⁰	0.5641	1.06E ⁻¹¹	7.75E ⁻¹¹	0.708	2.59E ⁻¹²	6.62E ⁻¹³	1.0327	2.22E ⁻¹²	1.49E ⁻¹²	1.090
S2	3.16E ⁻¹²	1.02E ⁻¹⁰	0.5701	6.61E ⁻¹²	3.86E ⁻¹¹	0.687	2.89E ⁻¹²	2.39E ⁻¹²	1.0846	2.49E ⁻¹²	1.22E ⁻¹³	1.004
S3	1.81E ⁻¹²	1.52E ⁻¹⁰	0.5383	2.62E ⁻¹²	1.27E ⁻¹⁰	0.555	7.10E ⁻¹³	1.08E ⁻¹²	1.0471	1.35E ⁻¹²	3.35E ⁻¹²	1.156
S4	7.45E ⁻¹²	8.08E ⁻¹¹	0.6639	1.28E ⁻¹¹	3.48E ⁻¹¹	0.795	2.31E ⁻¹²	7.95E ⁻¹³	1.0225	2.60E ⁻¹²	4.51E ⁻¹⁴	0.996
S5	1.85E ⁻¹²	5.02E ⁻¹⁰	0.48	1.01E ⁻¹¹	2.78E ⁻¹⁰	0.580	7.14E ⁻¹²	-2.13E ⁻¹²	0.9502	4.96E ⁻¹²	3.77E ⁻¹²	1.085
S6	3.77E ⁻¹³	2.70E ⁻¹⁰	0.4599	1.05E ⁻¹¹	7.99E ⁻¹¹	0.693	3.19E ⁻¹²	1.69E ⁻¹²	1.0466	2.51E ⁻¹²	1.69E ⁻¹³	1.006

uptake.

3.3.2. Model comparison and best fitting model selection

Fig. 6 summarizes the error set generated by all the analytical solutions, averaging the different tests. It highlights the minimum and maximum absolute error made over time, the median, and the interval of the first and third quartiles.

Even though all solutions generate low errors, the LDF and FD_{SW} make the highest errors in simulating the regeneration phase. Instead, the FD and FD_{RH} are less accurate in estimating sorption. The LDF_{DW} variant is the one that makes, on average (over time and along different experiments), the smallest absolute error. For this reason, it is considered the best-fitting model for this hydrogel family. Successive analyses are thus based on this model.

Section A4 of supplementary information reports the dynamic error analysis results graph over time for each model, test, and sample.

3.4. Influence of temperature and water uptake on effective diffusivity

The best-fitting model (LDF_{DW}) has demonstrated that the diffusivity in the studied compositions exhibits an effective value in the order of 10^{-11} m²/s and a sensible dependence on water uptake (Fig. 7a) and temperature (Fig. 7b).

The effective diffusivity of water vapor exhibits comparable values in silica gel and zeolites (10^{-11} m²/s [18,76,77,82,83]) and in swelling polymers such as PEBAX [84,85] with equivalent water contents. Different findings emerge in highly hydrated PAM [40,45,75] studies, where water diffusivity varies significantly, ranging from 10^{-8} to 10^{-6} m²/s. The higher water mobility is presumably associated with the liquid diffusion within the polymeric network. This diffusion is facilitated by the hydrogen-bonding networks available when the sorbent

maintains a saturated level [40,45,86].

In this case, the water chemical potential within the polymer network impacts water mobility and diffusive resistance rather than the vapor pressure gradient across microporosity. This mechanism is proportional to local water concentration [40,45,86].

In our study, the dependence of effective diffusivity from water concentration, shown in Fig. 7a, presumes the presence of a transport mechanism similar to liquid diffusion within the polymeric network, then proportional to water content. However, being the water content 50 % less than in the study based on PAM, the influence of liquid diffusion is reduced, and the resulting value is more comparable to a conventional sorbent.

On the other hand, the temperature dependence shown in Fig. 7b follows a typical Arrhenius behavior. As temperature increases, the kinetic energy of water molecules also increases, leading to faster diffusion through the material's structure [18].

To include the latter aspect in the model, the coefficients a and b are written as functions of temperature using experimental data. This approach allows to simulate sorption and desorption kinetics at different temperatures. The inclusion of the temperature dependence on $a(T)$ and $b(T)$ transforms Eq. (13) in Eq. (16):

$$\frac{w(t) - w_0}{w_{eq} - w_0} = \frac{e^{\frac{F_0(a(T)+b(T) \cdot w_{eq})}{R_p^2} \cdot t}}{e^{\frac{F_0(a(T)+b(T) \cdot w_{eq})}{R_p^2} \cdot t} + b(T) \cdot \left(\frac{w_{eq} - w_0}{a(T) + b(T) \cdot w_0} \right)} - 1 \quad (16)$$

The fitted coefficients a and b for the studied tests change with temperature, respectively, linearly and exponentially. This approach allowed us to approximate the functional dependence of D on temperature T as follows: $D(w) = a(T) + b(T) \cdot w(t)$, with $a(T) = v_1 + v_2(T + 273.15)$ and $b(T) = v_3 \exp(-v_4/(T + 273.15))$, being T expressed in degrees Celsius. The coefficients v_1 , v_2 , v_3 , and v_4 are the results of a least square method fitting methodology on the fitted coefficients a and b , the same procedure explained in Section 2.4. The resulting values for sample S1 are $v_1 = -1.95 \times 10^{-11}$ m²/s, $v_2 = 7.48 \times 10^{-14}$ 1/K, $v_3 = 2.03 \times 10^{-2}$ m²/s, $v_4 = 7.30 \times 10^3$ K. Fitting results for all the remaining samples are in section A3 of supplementary information.

In conclusion, the general expression of $w(t)$, including the influence of the operative temperature of the sorbent, is:

$$\left\{ \begin{aligned} \frac{w(t, T) - w_0}{w_{eq} - w_0} &= \frac{e^{\frac{F_0 \cdot D_{eq} \cdot t}{R_p^2}} - 1}{e^{\frac{F_0 \cdot D_{eq} \cdot t}{R_p^2}} + v_3 \cdot e^{-\frac{v_4}{T+273.15}} \cdot \left(\frac{w_{eq} - w_0}{D_0} \right)} \\ D_{eq} &= D(w_{eq}, T) = v_1 + v_2 \cdot (T + 273.15) + v_3 \cdot e^{-\frac{v_4}{T+273.15}} \cdot w_{eq} \\ D_0 &= D(w_0, T) = v_1 + v_2 \cdot (T + 273.15) + v_3 \cdot e^{-\frac{v_4}{T+273.15}} \cdot w_0 \end{aligned} \right. \quad (17)$$

3.5. Determination of the optimal cycle

The best-fitting model from eq.(17) is used to study the performance of the sorbent when cycled between sorption and regeneration, determining the optimal time at a specific temperature and RH. In practical applications involving atmospheric water vapor harvesting, the thermal

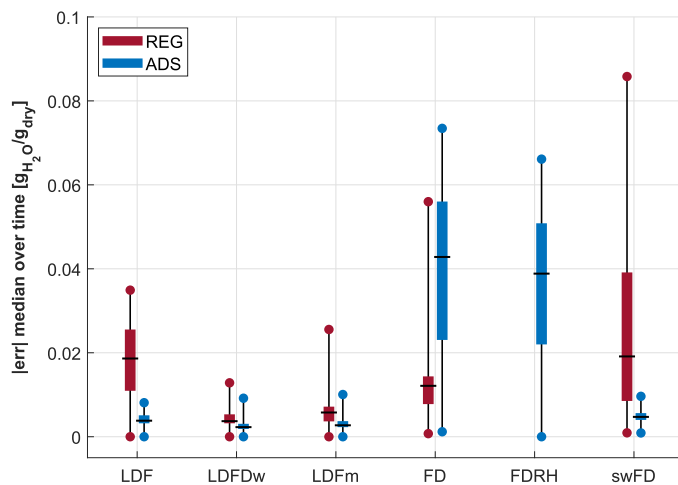


Fig. 6. Average of the instantaneous error generated by each model and categorized by the model typology. Each error bar contains the error distribution evaluated for all the samples.

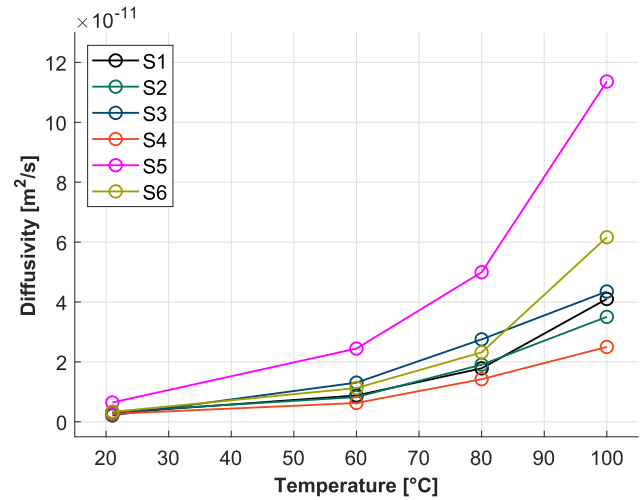
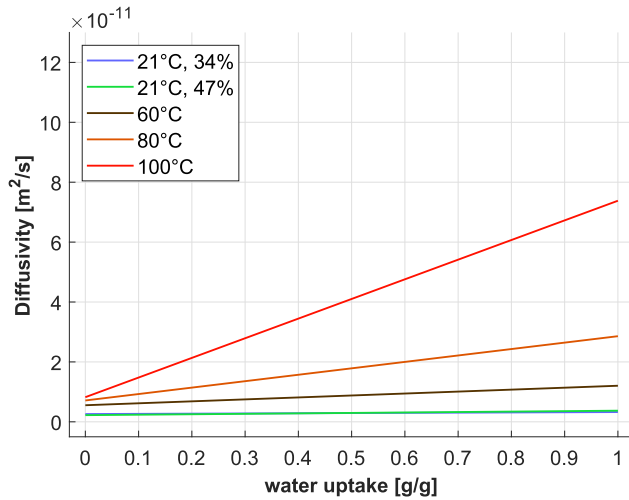


Fig. 7. a) Dependence of sample S1 diffusivity on water uptake at different temperatures. b) Dependence of D on the temperature at a fixed water uptake (0.5 g/g, as a reference) for all samples.

cycle often consists of short fixed durations repeated throughout the day. Consequently, the sorbent may not reach equilibrium conditions over several cycles.

This study optimized the durations of the regeneration/sorption cycle to ensure that an equivalent water mass is released and captured during regeneration ($\Delta w_{ads} = \Delta w_{reg}$). This approach stabilizes final uptakes after adsorption and regeneration at fixed values.

When the water uptake variation Δw is equal to the equilibrium value, as in sorption isotherms, the material exploits its maximum potential (w_{eq}). However, the regeneration or sorption phases require a duration equivalent to equilibration time (several hundred minutes), leading to low Δw rates or daily water yields. On the contrary, reducing cycle times can increase the Δw rate, obtaining an optimal trade-off.

Many variables influence the problem of finding the optimal, and identifying a single solution requires a parametrical approach. Imposing a maximum acceptable percentage of the maximum water uptake potential, i.e., Δw_{max} is 70 % of the equilibrium value w_{eq} , the problem

depends only on T_{ads} , T_{reg} , and RH_{ads} .

Fig. 8a reports as an example the cycle duration and the Δw variation over time when 75 °C is the regeneration temperature, while 21 °C and 50 % are temperature and relative humidity during sorption.

Increasing the regeneration time (from 10 to 60 min), the Δw during regeneration increases, but it requires a longer sorption time to re-equilibrate the water uptake to its initial value (70 % of the w_{eq}), obtaining the cycle symmetry of $\Delta w_{ads} = \Delta w_{reg}$. Hence, the variation of the regeneration time influences the value of the Δw rate.

Fig. 8b reports the behavior of Δw rate as a function of regeneration time and for maximum water uptake potential between 20 % and 90 % of w_{eq} .

For w_{max}/w_{eq} less than 40 %, the Δw rate has a monotonic quasi-linear decrescent behavior.

For w_{max}/w_{eq} higher than 40 %, the Δw rate curves show a local maximum that shifts towards higher regeneration times as w_{max} / w_{eq} increases from 40 % to 90 %. The figure illustrates that the Δw rate

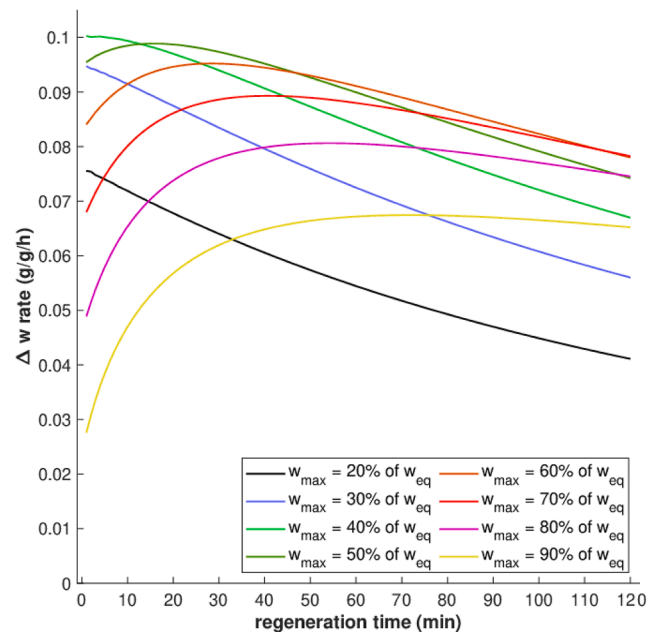
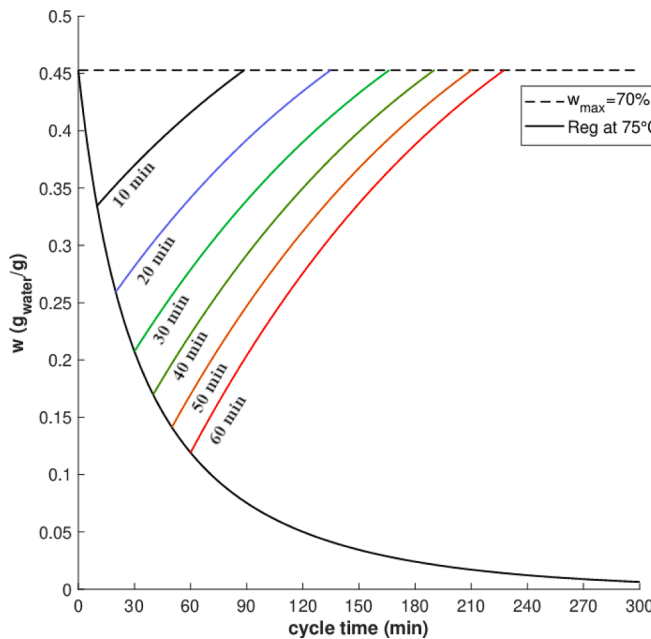


Fig. 8. a) Settled cycling curves (simulated through LDF_{Dw} for regeneration at 75 °C and sorption at 21 °C and $RH=50\%$) at different fixed regeneration times, and for sample S6-Alg₁Ca₅G_{0.025}; b) the water uptake rate (Δw_{rate}) plotted against each chosen regeneration time for different initial water uptakes expressed as a fraction of the equilibrium value.

reaches its peak values (within 0.09–0.1 g/g/h) when regeneration time is below 35 min, and the maximum water uptake potential is within 40–70 % of the equilibrium value.

Parametric repetition of the approach depicted in Fig. 8 for each influencing variable generates the water productivity maps shown in Fig. 9. In particular, regeneration temperatures spanned 60–100 °C, RH equal to 30 % and 50 %, and the w_{eq} ranged between 20 % and 90 % of its maximum value.

The contour lines delineate specific functioning zones, each corresponding to a distinct hourly water productivity as Fig. 8 defines the Δw rate (g/g/hour).

The maps illustrate that the region with the highest water productivity is commonly situated within a w_{eq} range of 40–50 % range and a regeneration time under 35 min. With an RH of 30 %, the water productivity rises from 0.065 to 0.09 kg_{water}/kg_{Alg}/hour as the regeneration temperature increases from 60 to 100 °C. Over a 24-h operational period, the daily productivity ranges between 1.56 and 2.16 kg_{water}/kg_{Alg}/day. These values escalate to 2–2.9 kg_{water}/kg_{Alg}/day under an RH of 50 %.

Most of the studies from the literature [24,31,32,2,37,40,45] demonstrated lower performances than the findings of this study under similar ambient and regeneration conditions.

Only two studies declare sorbent configurations with higher daily productivity. The first, a PAM with MIL101(Cr) [42] and impregnated with CaCl₂ (14 %), achieved a daily water yield of 4.2 L/kg/day. However, results refer to a humid environment (RH ~ 90 %). When humidity is 30–50 %, the daily water production does not exceed 1 l/kg/day. The second configuration exploits a polyzwitterionic polymer PDMAAPS impregnated with LiCl (15 %) [47], achieving remarkable water productivity of 5.6 L/kg/day at low humidity.

4. Conclusions

This experimental and theoretical study showcases the efficacy of utilizing a composite hydrogel based on Calcium Alginate combined with natural graphite to facilitate fast and frequent sorption/

regeneration cycles for atmospheric water harvesting applications. The main findings can be summarized as follows:

- The composition of the hydrogel significantly influences its sorption capacity and kinetics. Lower levels of sodium alginate and higher amounts of calcium chloride enhance the equilibrium water uptake, while the addition of graphite improves desorption kinetics. However, excessive graphite concentrations may lead to porosity occlusion and generate adverse effects. Further optimization studies and analysis are required.
- Models based on the Linear Driving Force (LDF) approach demonstrate superior fitting with dynamic experimental results. Effective diffusivity derived from LDF models strongly depends on sorbent water concentration and temperature (an Arrhenius-like relationship) in sorption and regeneration. However, ambient RH does not affect diffusivity.
- The validated LDF_{DW} model provides predictions of the material's behavior with the best accuracy under thermal cycling within the operational temperature range of 20–100 °C. Model calibration requires only a few kinetics tests of regeneration/sorption to provide a good system and component design tool.
- In a low humidity environment (30–50 % RH), a regeneration time below 35 min optimizes the water uptake rate. Future studies must include the role of convection on mass transfer to improve the prediction of material performance under various operative conditions.
- The optimized LDF_{DW} cycle demonstrated a water daily productivity of 1.6–2.2 L/kg_{hydrogel}/day when RH is 30% (dry environment) and 2–2.9 liters/kg_{hydrogel}/day when RH is 50% with regeneration temperatures compatible with solar thermal applications or waste heat (60–100 °C).
- Despite the very low amount of CaCl₂ used (5% wt) for sodium alginate crosslinking, the biopolymer achieved better uptakes and water daily productivity than most materials studied in the literature. Studying the material behavior at higher hydrated states, e.g., at higher salt concentrations, can further increase performance of the sorbent material.

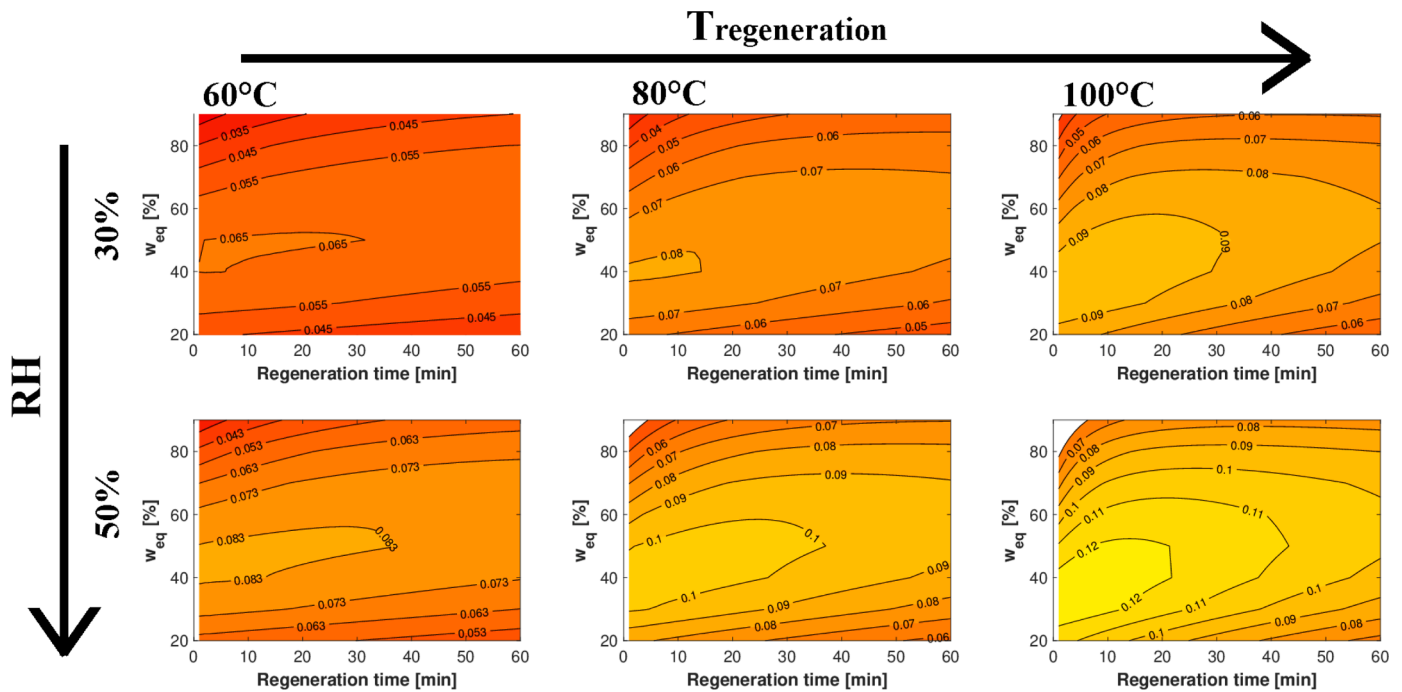


Fig. 9. The water productivity map for the CaAlg-graphite polymer is presented as a function of regeneration temperature (ranging from 60 °C to 100 °C) and ambient relative humidity (varying from 30% to 50%). Contour lines within each graph delineate the hourly water productivity per unit mass of sorbent (kg/kg/hour). The percentage of w_{eq} is depicted on the y-axis of each graph, while the x-axis represents the regeneration time of the cycle.

CRediT authorship contribution statement

Vincenzo Gentile: Conceptualization, Data curation, Funding acquisition, Investigation, Methodology, Modeling, Supervision, Visualization, Writing – original draft, Writing – review & editing. **Matteo Calò:** Data curation, Modeling, Visualization, Writing – original draft, Writing – review & editing. **Michael Bozlar:** Investigation, Writing – review & editing. **Marco Simonetti:** Funding acquisition, Writing – review & editing. **Forrest Meggers:** Funding acquisition, Writing – review & editing.

Declaration of Competing Interest

We confirm that the manuscript has been read and approved by all named authors and that there are no other persons who satisfied the criteria for authorship but are not listed. We further confirm that all have approved the order of authors listed in the manuscript of us.

We confirm that we have given due consideration to the protection of intellectual property associated with this work and that there are no impediments to publication, including the timing of publication, concerning intellectual property. In so doing, we confirm that we have followed the regulations of our institutions concerning intellectual property.

The authors Vincenzo Gentile, Forrest Meggers, Marco Simonetti, and Michael Bozlar have an international patent issued to Politecnico di Torino and Princeton University named “*Heat and mass exchanger made with alginate-bentonite biocomposite hydrogel for water vapor capture.*”

The authors Vincenzo Gentile, Forrest Meggers and Marco Simonetti reports financial support was provided by *Schmidt Transformative Technology Fund at Princeton University*.

The authors Vincenzo Gentile and Marco Simonetti reports financial support was provided by *PoC Instrument* initiative implemented by *LINKS*, *LIFTT*, and the *Compagnia di San Paolo* in Turin.

We understand that the Corresponding Author is the sole contact for the Editorial process (including Editorial Manager and direct communications with the office). He is responsible for communicating with the other authors about progress, submissions of revisions, and final approval of proofs. We confirm that we have provided a current, correct email address which is accessible by the Corresponding Author, and which has been configured to accept email from: vincenzo.gentile@polito.it

Data availability

Data will be made available on request.

Acknowledgments

The authors acknowledge support from the Schmidt Transformative Technology Fund at Princeton University. Additional support was provided by the PoC Instrument initiative implemented by LINKS, LIFTT, and the Compagnia di San Paolo in Torino, Italy.

Supplementary materials

Supplementary material associated with this article can be found, in the online version, at [doi:10.1016/j.ijheatmasstransfer.2023.124794](https://doi.org/10.1016/j.ijheatmasstransfer.2023.124794).

References

- [1] Wahlgren, R.V. Atmospheric water vapour processor designs for potable water production : a review, *Water Research* 35, (2001) 1–22. An update to this article is included at the end review paper 35, 2607–2614 (2001).
- [2] W. Wang, et al., Viability of a practical multicyclic sorption-based water harvester with improved water yield, *Water Res.* 211 (2022), 118029.
- [3] M. Ejeian, R.Z. Wang, Adsorption-based atmospheric water harvesting, *Joule* 5 (2021) 1678–1703.
- [4] K.K. Hyunho, et al., Water harvesting from air with metal-organic frameworks powered by natural sunlight, *Science* 434 (2017) 430–434.
- [5] B. Tashtoush, A. Alshoubaki, Atmospheric water harvesting : a review of techniques, performance, renewable energy solutions, and feasibility, *Energy* 280 (2023), 128186.
- [6] Y. Tu, R. Wang, Y. Zhang, J. Wang, Progress and expectation of atmospheric water harvesting, *Joule* 2 (2018) 1452–1475.
- [7] A. LaPotin, H. Kim, S.R. Rao, E.N. Wang, Adsorption-based atmospheric water harvesting: impact of material and component properties on system-level performance, *Acc. Chem. Res.* 52 (2019) 1588–1597.
- [8] G. Raveesh, R. Goyal, S.K. Tyagi, Advances in atmospheric water generation technologies, *Energy Convers. Manag.* 239 (2021), 114226.
- [9] H. Kim, et al., Adsorption-based atmospheric water harvesting device for arid climates, *Nat. Commun.* 9 (2018) 1–8.
- [10] R. Tu, Y. Hwang, Reviews of atmospheric water harvesting technologies, *Energy* 201 (2020), 117630.
- [11] D. Milani, A. Abbas, A. Vassallo, M. Chiesa, D. Al Bakri, Evaluation of using thermoelectric coolers in a dehumidification system to generate freshwater from ambient air, *Chem. Eng. Sci.* 66 (2011) 2491–2501.
- [12] M. Eslami, F. Tajeddini, N. Etaati, Thermal analysis and optimization of a system for water harvesting from humid air using thermoelectric coolers, *Energy Convers. Manag.* 174 (2018) 417–429.
- [13] N. Pokorny, V. Shemelin, J. Novotny, Experimental study and performance analysis of a mobile autonomous atmospheric water generator designed for arid climatic conditions, *Energy* 250 (2022), 123813.
- [14] M.G. Gado, M. Nasser, A.A. Hassan, H. Hassan, Adsorption-based atmospheric water harvesting powered by solar energy: comprehensive review on desiccant materials and systems, *Process Saf. Environ. Prot.* 160 (2022) 166–183.
- [15] M. Bilal, et al., Adsorption-based atmospheric water harvesting: a review of adsorbents and systems, *Int. Commun. Heat Mass Transf.* 133 (2022), 105961.
- [16] J.Y. Wang, R.Z. Wang, Y.D. Tu, L.W. Wang, Universal scalable sorption-based atmosphere water harvesting, *Energy* 165 (2018) 387–395.
- [17] J.N. Israelachvili, *Intermolecular and Surface Forces*, 2011.
- [18] D.M. Ruthven, *Principles of Adsorption and Adsorption processes*, John Wiley & Sons, 1984.
- [19] S. Lattemann, T. Höpner, Environmental impact and impact assessment of seawater desalination, *Desalination* 220 (2008) 1–15.
- [20] S. Miller, H. Shemer, R. Semiat, Energy and environmental issues in desalination, *Desalination* 366 (2015) 2–8.
- [21] T.M. Missimer, R.G. Maliva, Environmental issues in seawater reverse osmosis desalination: intakes and outfalls, *Desalination* 434 (2018) 198–215.
- [22] A. Subramani, J.G. Jacangelo, Emerging desalination technologies for water treatment: a critical review, *Water Res.* 75 (2015) 164–187.
- [23] A. Agrawal, A. Kumar, A.D. Parekh, Atmospheric water harvesting by using evacuated tube collector: an experimental investigation, *Appl. Therm. Eng.* 232 (2023), 121087.
- [24] M. Ejeian, A. Entezari, R.Z. Wang, Solar powered atmospheric water harvesting with enhanced LiCl/MgSO₄/ACF composite, *Appl. Therm. Eng.* 176 (2020), 115396.
- [25] A. Entezari, M. Ejeian, R. Wang, Modifying water sorption properties with polymer additives for atmospheric water harvesting applications, *Appl. Therm. Eng.* 161 (2019), 114109.
- [26] S. Bai, et al., Adsorption-based atmospheric water harvesting by passive radiative condensers for continuous decentralized water production, *Appl. Therm. Eng.* 225 (2023) 1–13.
- [27] V. Gentile, M. Bozlar, F. Meggers, M. Simonetti, Liter-scale atmospheric water harvesting for dry climates driven by low temperature solar heat, *Energy* 254 (2022), 124295.
- [28] Qiaoxin Zhang, M.L. Rang Tu, Performance analyses and optimization studies of desiccant wheel assisted atmospheric water harvesting system under global ambient conditions, *Energy* 283 (2023) 100137, <https://doi.org/10.1016/j.energy.2023.128477>.
- [29] B. Chaitanya, V. Bahadur, A.D. Thakur, R. Raj, Biomass-gasification-based atmospheric water harvesting in India, *Energy* 165 (2018) 610–621.
- [30] H. Maher, T.H. Rupam, K.A. Rocky, R. Bassiouny, B.B. Saha, S. silica gel-MIL 100(Fe) composite adsorbents for ultra-low heat-driven atmospheric water harvester, *Energy* 238 (2021), 121741.
- [31] H. Park, et al., Enhanced Atmospheric Water Harvesting with Sunlight-Activated Sorption Ratcheting, *ACS Appl. Mater. Interfaces* 14 (2022) 2237–2245.
- [32] H. Kim, et al., Water harvesting from air with metal-organic frameworks powered by natural sunlight, *Science* 356 (2017) 430–434.
- [33] M. Wang, et al., Solar-powered nanostructured biopolymer hygroscopic aerogels for atmospheric water harvesting, *Nano Energy* 80 (2021), 105569.
- [34] J.Y. Wang, J.Y. Liu, R.Z. Wang, L.W. Wang, Experimental research of composite solid sorbents for fresh water production driven by solar energy, *Appl. Therm. Eng.* 121 (2017) 941–950.
- [35] R. Li, et al., Hybrid hydrogel with high water vapor harvesting capacity for deployable solar-driven atmospheric water generator, *Environ. Sci. Technol.* 52 (2018) 11367–11377.
- [36] R. Li, Y. Shi, M. Wu, S. Hong, P. Wang, Photovoltaic panel cooling by atmospheric water sorption–evaporation cycle, *Nat. Sustain.* 3 (2020) 636–643.
- [37] R. Li, Y. Shi, M. Wu, S. Hong, P. Wang, Improving atmospheric water production yield: enabling multiple water harvesting cycles with nano sorbent, *Nano Energy* 67 (2020), 104255.

- [38] A. Permyakova, et al., Design of salt-metal organic framework composites for seasonal heat storage applications, *J. Mater. Chem. A* 5 (2017) 12889–12898.
- [39] K. Matsumoto, N. Sakikawa, T. Miyata, Thermo-responsive gels that absorb moisture and ooze water, *Nat. Commun.* 9 (2018) 1–7.
- [40] H. Lu, et al., Tailoring the desorption behavior of hygroscopic gels for atmospheric water harvesting in arid climates, *Adv. Mater.* (2022), 2205344.
- [41] P.A. Kallenberger, et al., Alginate-Derived Salt/Polymer Composites for Thermochemical Heat Storage, *Adv. Sustain. Syst.* 2 (2018) 1–8.
- [42] G. Yilmaz, et al., Autonomous atmospheric water seeping MOF matrix, *Sci. Adv.* 6 (2020) 1–9.
- [43] F. Zhao, et al., Super moisture-absorbent gels for all-weather atmospheric water harvesting, *Adv. Mater.* 31 (2019) 1–7.
- [44] A. Entezari, M. Ejeian, R. Wang, Super atmospheric water harvesting hydrogel with alginate chains modified with binary salts, *ACS Mater. Lett.* 2 (2020) 471–477.
- [45] J. Xu, et al., Ultrahigh solar-driven atmospheric water production enabled by scalable rapid-cycling water harvester with vertically aligned nanocomposite sorbent, *Energy Environ. Sci.* 14 (2021) 5979–5994.
- [46] M. Wu, et al., Metal- And halide-free, solid-state polymeric water vapor sorbents for efficient water-sorption-driven cooling and atmospheric water harvesting, *Mater. Horizons* 8 (2021) 1518–1527.
- [47] C. Lei, et al., Polyzwitterionic hydrogels for efficient atmospheric water harvesting, *Angew. Chem. - Int. Ed.* 61 (2022) 1–5.
- [48] P.A. Kallenberger, M. Fröba, Water harvesting from air with a hygroscopic salt in a hydrogel-derived matrix, *Commun. Chem.* 1 (2018) 1–6.
- [49] Y. Guo, et al., Hydrogels and Hydrogel-Derived Materials for Energy and Water Sustainability, *Chem. Rev.* 120 (2020) 7642–7707.
- [50] E.M. Ahmed, H. hydrogel: preparation, characterization, and applications: a review, *J. Adv. Res.* 6 (2015) 105–121.
- [51] S. Meng, H. Winters, Y. Liu, Ultrafiltration behaviors of alginate blocks at various calcium concentrations, *Water Res.* 83 (2015) 248–257.
- [52] K.Y. Lee, D.J.A. Mooney, Properties and biomedical applications, *Prog. Polym. Sci.* 37 (2012) 106–126.
- [53] M.N.V.R. Kumar, A review of chitin and chitosan applications, *React. Funct. Polym.* 46 (2000) 1–27.
- [54] J.L. Drury, D.J. Mooney, H. hydrogels for tissue engineering: scaffold design variables and applications, *Biomaterials* 24 (2003) 4337–4351.
- [55] N. Fatin-Rouge, et al., Removal of some divalent cations from water by membrane-filtration assisted with alginate, *Water Res.* 40 (2006) 1303–1309.
- [56] O. Ozay, S. Ekici, Y. Baran, N. Aktas, N. Sahiner, Removal of toxic metal ions with magnetic hydrogels, *Water Res.* 43 (2009) 4403–4411.
- [57] F. Ge, M.M. Li, H. Ye, B.X. Zhao, Effective removal of heavy metal ions Cd^{2+} , Zn^{2+} , Pb^{2+} , Cu^{2+} from aqueous solution by polymer-modified magnetic nanoparticles, *J. Hazard. Mater.* 211–212 (2012) 366–372.
- [58] X. Zhou, F. Zhao, Y. Guo, B. Rosenberger, G. Yu, Architecting highly hydratable polymer networks to tune the water state for solar water purification, *Sci. Adv.* 5 (2019) 1–8.
- [59] A. Mignon, et al., Alginate biopolymers: counteracting the impact of superabsorbent polymers on mortar strength, *Constr. Build. Mater.* 110 (2016) 169–174.
- [60] S. Xu, X. Liu, A. Tabaković, E. Schlangen, Investigation of the potential use of calcium alginate capsules for self-healing in porous asphalt concrete, *Materials (Basel)* 12 (2019) 1–13.
- [61] J. Wang, et al., Application of modified-alginate encapsulated carbonate producing bacteria in concrete: a promising strategy for crack self-healing, *Front. Microbiol.* 6 (2015) 1–14.
- [62] V. Gentile, M. Libralato, S. Fantucci, L. Shtrepi, G. Autretto, Enhancement of the hygroscopic and acoustic properties of indoor plasters with a super adsorbent calcium alginate biopolymer, *J. Build. Eng.* 76 (2023), 107147.
- [63] E. Caló, V.V. Khutoryanskiy, Biomedical applications of hydrogels: a review of patents and commercial products, *Eur. Polym. J.* 65 (2015) 252–267.
- [64] N.A. Peppas, P. Bures, W. Leobandung, H. Ichikawa, Hydrogels in pharmaceutical formulations, *Eur. J. Pharm. Biopharm.* 50 (2000) 27–46.
- [65] H. Mittal, A. Al Alili, S.M. Alhassan, M. Naushad, Advances in the role of natural gums-based hydrogels in water purification, desalination and atmospheric-water harvesting, *Int. J. Biol. Macromol.* 222 (2022) 2888–2921.
- [66] G. Skjåk-Bræk, H. Grasdalen, O. Smidsrød, Inhomogeneous polysaccharide ionic gels, *Carbohydr. Polym.* 10 (1989) 31–54.
- [67] P. Sikorski, F. Mo, G. Skjåk-Bræk, B.T. Stokke, Evidence for egg-box-compatible interactions in calcium - Alginate gels from fiber x-ray diffraction, *Biomacromolecules* 8 (2007) 2098–2103.
- [68] G.T. Grant, E.R. Morris, D.A. Rees, P.J.C. Smith, D. Thom, Biological interactions between polysaccharides and divalent cations: the egg-box model, *FEBS Lett.* 32 (1973) 195–198.
- [69] W. Plazinski, Molecular basis of calcium binding by polyguluronate chains. Revising the egg-box model, *J. Comput. Chem.* 32 (2011) 2988–2995.
- [70] L. Li, Y. Fang, R. Vreeker, I. Appelqvist, E. Mendes, Reexamining the egg-box model in calcium - Alginate gels with X-ray diffraction, *Biomacromolecules* 8 (2007) 464–468.
- [71] S.N. Pawar, K.J. Edgar, A. Alginate derivatization: a review of chemistry, properties and applications, *Biomaterials* 33 (2012) 3279–3305.
- [72] S.K. Bajpai, S. Sharma, Investigation of swelling/degradation behaviour of alginate beads crosslinked with Ca^{2+} and Ba^{2+} ions, *React. Funct. Polym.* 59 (2004) 129–140.
- [73] S.K. Motwani, et al., Chitosan-sodium alginate nanoparticles as submicroscopic reservoirs for ocular delivery: formulation, optimisation and in vitro characterisation, *Eur. J. Pharm. Biopharm.* 68 (2008) 513–525.
- [74] J. Crank, The mathematics of diffusion, *Journal of the American Chemical Society (Clarendon press Oxford)* (1975), <https://doi.org/10.1021/ja01562a072>.
- [75] C.D. Díaz-Marín, et al., Heat and mass transfer in hygroscopic hydrogels, *Int. J. Heat Mass Transf.* 195 (2022).
- [76] E. Glueckauf, Theory of chromatography, *Trans. Faraday Soc.* 51 (1955) 1540–1551.
- [77] Y.I. Aristov, M.M. Tokarev, A. Freni, I.S. Glaznev, G. Restuccia, Kinetics of water adsorption on silica Fuji Davison RD, *Microporous Mesoporous Mater.* 96 (2006) 65–71.
- [78] I.I. El-Sharkawy, On the linear driving force approximation for adsorption cooling applications, *Int. J. Refrig.* 34 (2011) 667–673.
- [79] P.J. Bickel, K.A. Doksum, *Mathematical Statistics Basic Ideas and Selected Topics*, I, Taylor & Francis Group, 2015.
- [80] J.A. Nelder, R. Mead, A simplex method for function minimization, *Comput. J.* 7 (1965) 308–313.
- [81] J.C. Lagarias, J.A. Reeds, M.H. Wright, P.E. Wright, Convergence properties of the Nelder-Mead simplex method in low dimensions, *SIAM J. Optim.* 9 (1998) 112–147.
- [82] M. Simonetti, et al., Experimental testing of the buoyant functioning of a coil coated with SAPO34 zeolite, designed for solar DEC (Desiccant Evaporative Cooling) systems of buildings with natural ventilation, *Appl. Therm. Eng.* 103 (2016) 781–789.
- [83] M. Simonetti, V. Gentile, L. Liggieri, G.V. Fracastoro, M.G. Carrabba, Experimental analysis of “NAC-wall” for hybrid ventilation mode, *Energy Build.* 152 (2017) 399–408.
- [84] J. Potreck, K. Nijmeijer, T. Kosinski, M. Wessling, Mixed water vapor/gas transport through the rubbery polymer PEBAX® 1074, *J. Memb. Sci.* (2009), <https://doi.org/10.1016/j.memsci.2009.03.051>.
- [85] J. Pantelic, E. Teitelbaum, M. Bozlar, S. Kim, F. Meggers, Development of moisture absorber based on hydrophilic nonporous membrane mass exchanger and alkoxylated siloxane liquid desiccant, *Energy Build.* 160 (2018) 34–43.
- [86] C. Yan, P.L. Kramer, R. Yuan, M.D. Fayer, Water dynamics in polyacrylamide hydrogels, *J. Am. Chem. Soc.* 140 (2018) 9466–9477.